Article:
Dangnan, F, Espejo, C, Liskiewicz, T et al. (2 more authors) (2021) Water barrier performance of additively manufactured polymers coated with diamond-like carbon films. Diamond and Related Materials, 119. 108541. ISSN 0925-9635

https://doi.org/10.1016/j.diamond.2021.108541

Water barrier performance of additively manufactured polymers coated with diamond-like carbon films

F. Dangnan[a*], C. Espejo, T. Liskiewicz[b], M. Gester[c], A. Neville[a]
*pm12fd@leeds.ac.uk

[a]*Institute of Functional Surfaces (iFS), School of Mechanical Engineering, University of Leeds, Leeds, LS2 9JT, UK*
[b]*Manchester Metropolitan University, Faculty of Science and Engineering, Manchester M15 6BH, UK*
[c]*P&G Reading Innovation Centre, 460 Basingstoke Road, Reading, RG2 0QE, UK*

Keywords

Additive manufacturing; Polyjet technology; DLC coating; Barrier film; WVTR; Water permeation

Abstract

While additive manufactured polymers have unique and useful properties, the deficiency of water barrier performance limits their shelf-life and functionality as a diffusion barrier for long life product durability. In this work, the induced modification of diamond-like carbon (DLC) coatings using nitrogen (N) (up to 2.02 at. %) to improve water barrier performance has been studied. DLC thin films were deposited onto additively manufactured polymers: acrylonitrile butadiene styrene (3D ABS) and Verogray polymers using microwave-plasma enhanced chemical vapour deposition (MW-PECVD) technique. Test results are described for two N-doped DLC films (a-C:N:H): DLC-1 and DLC-2 deposited at temperatures below 40 °C. Techniques such as Fourier-transform infrared spectroscopy (FTIR), atomic force microscopy (AFM), Raman spectroscopy, mercury injection capillary pressure (MICP) measurement and nanoindentation were utilised to study both material and film properties. A good correlation between film thickness and water barrier function for 3D ABS was found. However, for the Verogray samples, film thickness played a limited role in reducing the WVTR. Distinguishable microstructural pit-like defects present on the 3D ABS substrate were seen to promote a higher WVTR of 73.31 g/m^2-day for the 3D ABS uncoated samples as compared with 28.8 g/m^2-day for Verogray. The result from this test show strong evidence that DLC coatings could serve as a good water vapour barrier in additively manufactured polymer systems where polymer-water vapour contact may be required, especially in the packaging and food industry where modified atmospheric packaging may be required.

1. Introduction

The combination of polymer-based material (PBM) with functional and protective coatings provide key advantages over alternative bulk material in product design where complex shapes are required for specific design roles to achieve lightweight materials, design freedom, and barrier functions [1]. Additive manufacturing (AM) has seen increasing research effort to better understand and improve material performance with several corresponding technologies to improve product resolution, surface finish, mechanical properties and barrier functions. Polymers, in general, have widely been used in various sections of product manufacturing. However, due to their limitations in performance when exposed to light or water vapour, they tend to function poorly when compared with both glass and metals [2], especially when their barrier properties are the subject of interest. Epoxies and other chain containing functionalities have shown greater susceptibility to degradation when exposed to ultraviolet light and water [3]. Degradation caused by hydrolysis leading to the formation of ammonia, phosphoric acid and other corresponding side groups has been reported by numerous authors [4, 5, 6]. Several organic barrier coatings such as polyacrylonitrile (PAN) and ethylene vinyl alcohol (EVOH) have been developed with significantly improved barrier functionality over the commonly used polyethylene terephthalate (PET) and polyethylene (PE) plastics [7]. The performance of EVOH is claimed to be 10,000 times superior to PE, with barrier function (for water vapour and most gases) as low as 1cm^3/m^2-day for a 20 µm film [8]. However, at relative humidity values greater than 70 %, these organic-based coatings become functionally defective against water vapour [8] and, as such, multi-laminate structures of the barrier coating are needed to compensate for the low barrier performance, thus making the procedure very expensive and unreliable to some extent [7]. This becomes even more complex when AM polymers are involved, as barrier property layers cannot be effectively manufactured using AM techniques. Hence, special coating methods must be adopted to provide specific barrier function for both water and gases.

Inorganic coatings such as diamond-like carbon (DLC) has become popularly used in recent times for improved barrier performance on polymers substrates [7], for example, in the food and packaging industry [9]. Several authors have demonstrated the practical use of DLC films on non-3D printed polymer substrates to highlight these properties [9, 10]. Abbass *et al.* [10], in the use of DLC coating for the purposes of achieving improved barrier function for PET polymer, demonstrated a 65.23 % reduction in the WVTR for a 1.61g/m^2-day permeation rate for the pristine polymer. However, one major drawback with the use of DLC coating is the possession of high intrinsic compressive stress that can reach several GPa and may cause stress cracking in the coating and alter coating adhesion performance resulting in coating delamination. To this end, alternative processes including elemental doping using N or Si has been studied to reduce the compressive stress build-up within the coating structure by improving coating adhesion, mechanical performance and barrier function [11]. Ray *et al.* [12] showed that the effect of nitrogen doping on a-C:H films has a positive correlation to the WVTR performance. They further observed that, by increasing the gas flow rate for nitrogen from 5 sccm (standard cubic centimetre per min) to 20 sccm, an ~ 8 % and ~ 12 % reduction in the WVTR was observed for the respective DLC coating structures deposited onto PET polymers.

Thin-film formation using chemical vapour deposition (CVD) is a high-temperature deposition process requiring temperatures in the range of 450 °C to 1050 °C, however, for physical vapour deposition (PVD), films are deposited at relatively low temperatures (~ 250 °C to 450 °C) [13]. These deposition temperatures on average are by far greater than most glass transition temperature (T_g) and melting temperatures (T_m) of many engineering polymers. Moulded ABS, for example, has a T_g of 105 °C and the situation is even more compromising for Polyjet additive manufactured ABS (3D ABS) material, with a T_g of 51 °C [14]. This means similar deposition conditions cannot be used for both substrates as this may result in severe structural defects or deformation (through melting or thermal degradation) of the AM polymer. Hence, the first task of any deposition process is to provide a coating method that minimizes the temperature upsurge during the process of thin-film formation. MW-PECVD has shown greater potential in this regard by reducing the thermal load on polymers with low T_g and T_m by allowing deposition at room temperatures whilst maintaining a higher deposition rate throughout the deposition cycle.

There is currently no work reported on the deposition of a-C:N:H DLC coatings on AM polymers synthesized by MW-PECVD at temperatures below 40 °C. This work focuses on providing a well-tailored and bespoke DLC coating produced using the MW-PECVD technique to achieve an advantageous combination of 3D printed polymer bulk properties with the particulate structural properties of a single layer DLC film to improve the mechanical and water vapour barrier function of the underlying additively manufactured substrate. Two contrasting DLCs with varying nitrogen gas flow rates were produced and deposited onto two Polyjet AM polymers namely digital ABS Plus (3D ABS) and Verogray. Their microstructure, mechanical properties, and chemical structural composition in relation to their WVTR functions have been studied.

2. Experimental details

2.1. Additive manufacturing

In this study, additively manufactured Polyjet parts: 3D ABS and Verogray grade polymers were chosen based on their physical, structural and chemical properties [14]. The liquid photopolymer resins for part printing were supplied by Stratasys USA. Computer-aided design (CAD) drawings for modelling the dimensions and sizes of the required sample to print were created using Solidworks®2017 and printed with a Polyjet® 1000 printer [15]. Table 1 provides a summary of the additively manufactured parts used in this work and the corresponding tests used in characterising both the uncoated and coated samples. In total, three different sample design shapes assigned as A, B and C were printed for DLC deposition. These design shapes were modelled and printed based on the individual requirement of the equipment and characterisation techniques used in this work [15].

Table 1- Substrate design types with dimension and characterisation methods.

Sample design type	Dimension	Characterisation techniques
A [disc shaped]	25mm (diameter) x 0.28mm (thickness)	WVTR, MICP
B [Rectangular shaped]	20mm x15mm x 2mm	Nanoindentation, SEM, FTIR, Raman
C [Rectangular shaped]	4.5mm x 5mm x 2mm	AFM, Talysurf profilometry, X-ray

2.2. DLC coating deposition process

Before deposition, a four-stage sample cleaning procedure was adopted to remove contaminants from the AM polymer surfaces originating from either the 3D printing process or from sample handling. The first stage involved mechanical removal of the support material used in the build platform, followed by a highly pressurised water blast treatment to further rid the surface of any remaining support material. Samples were later subjected to immersion in an ultrasonic bath of distilled water for 15 min followed by chemical treatment of ethanol and a 48-hr vacuum drying at 35 °C to rid the polymer of any adsorbed surface water during any of the pre-treatment procedures.

Samples were later wiped with a lint-free cloth dipped in ethanol before being mounted in the deposition chamber. To achieve maximum outgassing, samples were left under high vacuum at 1.2 x 10^{-5} mbar base pressure overnight at 35 °C. To further rid the surface of impurities and improve surface functionality and adhesion, a 3 min plasma surface etching (PSE) stage was utilised. With a maximum coil current of 100 A and a chamber pressure of 1.2 x 10^{-3} mbar, a 99.9 % argon plasma (50 sccm) was produced using a tungsten filament plasma cathodic source. The single-layer DLC films were deposited onto the three sample design types defined in Table 2 for 3D ABS and Verogray. For the DCL deposition run, a multi-purpose industrial scale Hauzer Flexicoat 850 system with MW-PECVD capability was used to deposit the DLC coatings. To form a high-quality micro-wave source plasma with good uniformity and step coverage, two micro-wave antennae (2.45 GHz) were both utilised to input energy into the working gas at 1.05 kW each.

With the added advantage of being easily tuneable to achieve the desired coating composition through careful manipulation of the feedstock gases, the MW-PECVD process has become popular for most reactive deposition systems [9]. Two distinct DLC coatings (DLC-1 and DLC-2 detailed further in Table 2) were produced using both argon (Ar) and acetylene (C_2H_2) as the discharge and precursor gases respectively. The different parameters are the nitrogen gas flow rate of 0 and 20 sccm and the deposition run time used for the individual coating steps. Thermocouples situated at the substrate table were utilised to prevent samples from exceeding the minimum glass transition temperature (T_g) of the most thermally sensitive polymer being Verogray, with a T_g of 46 °C in comparison with 56 °C for 3D ABS. Each process was made up of four deposition runs to allow adequate film thickness to develop, whilst maintaining deposition temperatures below 46 °C. A cooling step of 1 hr was introduced in-between deposition runs to allow for polymer relaxation and to prevent excessive temperature spike during deposition. The effect of nitrogen doping on the mechanical, structural, physical and moisture barrier performance of DLC films is discussed in the results section.

Table 2- Process parameters of DLC deposition.

DLC	MW Power (W)		Working Pressure (mbar)	C_2H_2 flow rate (sccm)	Ar flow rate (sccm)	N_2 flow rate (sccm)
	1	2				
1	1050	1050	0.012	610	50	-
2	1050	1050	0.012	610	50	20

2.3. Characterisation techniques

2.3.1. *Polymer substrate characterisation*

Mercury injection capillary pressure (MICP) measurement was employed to determine and characterize pore features, particularly pore throat size distribution in both 3D ABS and Verogray samples from the nano (< 1-3 nm) to the macroscale (up to 350µm). MICP is a fundamental technique allowing the pore size distribution to be characterised with great certainty within the nano to macro size pore range [16]. Surface characterisation at the nanoscale was investigated using a Bruker AXS SAS atomic force microscope (AFM) at a scan rate of 0.528 Hz. For both DLC coated and uncoated polymer surfaces, a scan area of 5 µm x 5 µm grid was used. To determine the surface roughness of the scanned surfaces, an AFM-NanoScope® Analysis x86_v190r1 software was utilised. All surface roughness data presented in this study are an average of three repeats.

2.3.2. *DLC coating characterisation*

Cross-section SEM images for measuring coating thickness were obtained using a cold field emission (CFE) SEM-Hitachi SU8230. A 10nm conductive layer of gold was deposited onto the polymer surface via magnetron sputtering before imaging. All coating thickness presented in this work is an average of three repeats to ensure reliability and repeatable data. The surface morphology of both coated and uncoated surfaces was also imaged using the SEM.

X-ray photoelectron spectroscopy (XPS) analysis of the two coatings was performed using a Thermo NEXSA XPS fitted with a monochromatic Al kα X-ray source (1486.7 eV), a spherical sector analyser and 3 multichannel resistive plates, 128 channel delay line detectors. All data was recorded at 19.2 W and an X-ray beam size of 200 x 100 µm. Survey scans were recorded at pass energy of 160 eV, and high-resolution scans recorded at pass energy of 20 eV. Electronic charge neutralization was achieved using a dual-beam low-energy electron/ion source (Thermo Scientific FG-03). Ion gun current was set at 150 µA, and ion voltage at 45 V. All sample data was recorded at a pressure below 10^{-8} Torr and a room temperature of 21 °C. Sample etching was performed using a MAGCIS source operating at 4 kV with monotomic Ar^+ ions and rastered over an area of ca 1 × 1 mm.

Fourier transform infrared (FTIR) spectroscopy has been fully exploited for the identification and characterization of the basic chemical structural units presented in all the 3D polymers under study. The comprehensive vibration band assigned to each of the polymers is presented for the selected Infrared (IR) peak for easy confirmation of their molecular structure. All the measurements were acquired using the Attenuated Total Reflectance (ATR) accessory coupled to a Perkin Elmer Spectrum 100 FTIR Spectrometer. The spectral data ranged from 600 to 4000 cm^{-1}, with a spectral resolution of 4 cm^{-1}.

Raman spectra were acquired to examine the chemical bonding state of the DLC films from 1000 cm^{-1} to 1800 cm^{-1} Raman shift and fitted by two Gaussian peaks. The coated samples were exposed to a 488 nm laser mounted in a Renishaw InVia Raman microscope. Analysis using a fixed maximum laser power output of 0.1 mW was used throughout the analysis with a 10 sec exposure time over 5 exposures to avoid damage. The integral intensity given by the I_D/I_G ratios were calculated from the ratio of the area under the curve of the *D* and *G* peaks, which is closely related to the sp^2/sp^3 carbon ratio of the MW-PECVD DLC films**.**

The stationary water contact angles (c.a) of the AM samples were examined using an optical contact angle goniometer (CAM 101 KSV Instrument) at ambient temperature (25 °C) to quantify the surface energy of the treated polymer surface bombarded with energetic Ar^+ species after plasma surface etching (PSE) using demineralised water (polar). Three replicate measurements were taken for each sample and the contact angles automatically determined using the Laplace-Young fitting algorithm. To minimise the effect of drop impact due to weight on the wettability values, the total volume of drop deposited on the sample surface was always less than 10 µl [17].

To access the individual coating adhesion, a Tribotechnic Millennium 200 scratch tester with a Rockwell C diamond tip with a radius of 200µm was used. A progressive linear load of 0-20 N with a loading speed of 10 N/min was employed. The scratch speed and length were 10 mm/min and 10 mm respectively. The critical load points (L_c) along the scratched length defined by L_c1, L_c2 and L_c3 (where L_c1, L_c2 and L_c3 are the initial, second and final critical loads respectively) were analysed.

2.4. Water vapour transmission rate measurement (WVTR)

The WVTR function of the DLC coated and uncoated 3D printed polymers were assessed using the MOCON PERMATRAN-W model 3/33 equipment according to ASTM F1249 standards. The test samples were first masked using a 100 mm diameter Aluminium (Al) foil mask to reduce the size of the test area. In all the experiments, the exposed area was reduced to 1 cm^2, to compare the obtained WVTR values under the same conditions. The samples preparation procedure for testing is schematically presented in Figure 1.

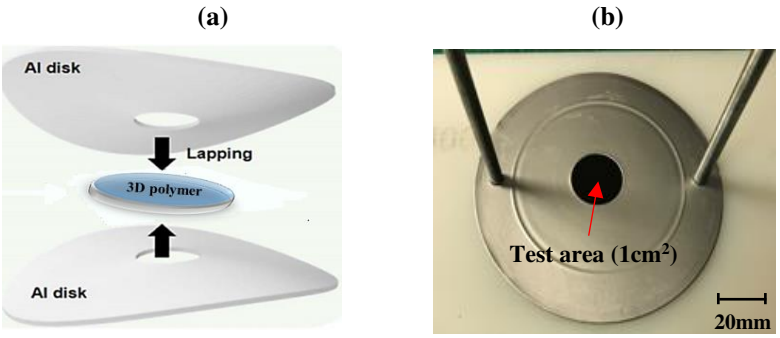

Figure 1- Fabrication procedure for masking the individual test samples for WVTR testing with (a) lapping of the individual test samples using Aluminium mask (b) test sample showing exposed test area of 1 cm^2 in black.

3. Results and discussion

3.1. Characterisation of additively manufactured parts

3.1.1. *Pore size characterisation*

An investigation into the pore size distribution of both 3D ABS and Verogray is shown in Figure 2. The plot reveals varying pore size radius and distribution function within the polymer matrix. For both samples, the minimum pore radius value is 0.0015 µm, which accounts for 19 and 12 % of the total void fraction for both 3D ABS and Verogray respectively. On the other hand, a maximum pore size radius of 3.6 and 0.9 µm was observed for the 3D ABS and Verogray polymers respectively, with corresponding percentages voidage of 4.4 x 10^{-5} and 5.5 x 10^{-5} %. It was further observed that both polymer pore size distribution lies between the meso (1-25 nm) and macropore (>25 nm) size characterization range [18] with varying pore distribution functions within the two limits as shown in Figure 2. The pore structure and classification further reveal the leading structural regime dominated by mesopore structures (1-25 nm). For 3D ABS, this percentage represents a total of 99.75 % of the total voidage, with the macropores (>25 nm) occupying only 0.25 % of the remaining pore volume. However, Verogray showed a slightly higher value for the mesopore fraction with a 20 % increase in the total void fraction occupied by the macropores, thus resulting in a fractional loss (< 0.6 %) of the total fraction of pores occupied by the mesopores. The percentage calculated fractions for both meso and macropores were 99.70 % and 0.30 % respectively. As a result, the porosity for both samples as determined by the MICP technique reflected a higher porosity of 7.7 % for 3D ABS as against a 6.6 % porosity value for Verogray. Wang *et al.* [19], in a similar study for polylactic acid (PLA), manufactured using fused deposition modelling (FDM), observed similar porosity values using both the upper and lower limits pore distribution function. In their work, however, they noted that over 99 % of the pore structure comprises macropores greater than 0.0388 nm for FDM manufactured PLA polymers.

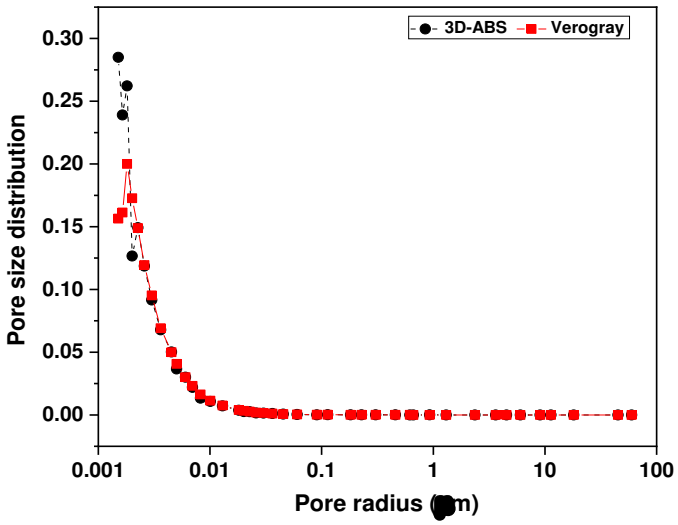

Figure 2- MICP plot showing the pore size distribution function against pore size radius for both 3D ABS and Verogray samples.

3.1.2. *FTIR spectra analysis*

FTIR spectra analysis for both 3D ABS and Verogray where the selected Infrared (IR) peaks for easy confirmation of their molecular structure [20] is shown in Figure 3. The characteristic large singlet –OH absorption peak, which occurs at wavenumbers between 3550 - 3200 cm^{-1} [21], is seen in both polymers with a much stronger peak observed with the Verogray sample. This observed peak may be attributed to the molecular vibration of the –OH structure present in H_2O at the polymer surface when exposed to the environment after printing. Apart from the IR peak intensity variations observed for the –OH band, similar vibration patterns were seen from wavenumbers 3000 cm^{-1} to 1500 cm^{-1} for all samples studied. Amongst the major peaks were the sp^3-CH stretching observed between 3000 - 2800 cm^{-1} wavenumbers, which are typical of aliphatic compounds, with additional CH_2 group vibration shown at 2918 cm^{-1} wavenumber for the asymmetric C-H vibration, and 2853 cm^{-1} symmetric C-H vibration [22]. As shown in Figure 3, the principal transmission signal observed between 2000 - 1500 cm^{-1} is due to C=O and C=C stretching, with C=C occurring around 1650 cm^{-1} due to its weak absorption properties [21].

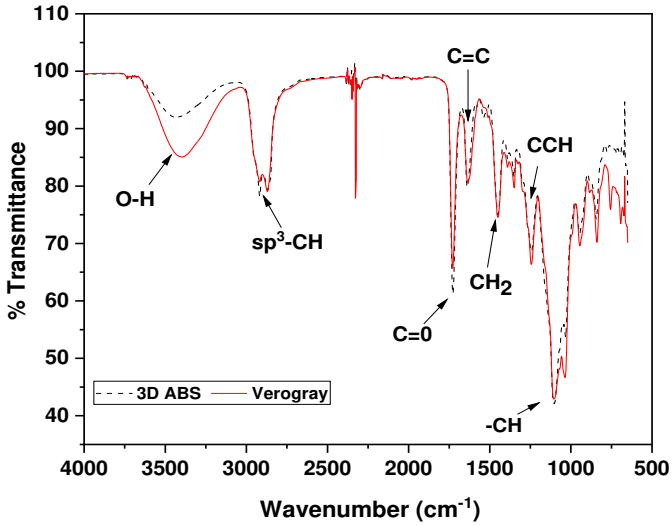

Figure 3- FTIR spectra plot of the 3D printed samples.

Surface wettability based on the measurement of the polymer c.a response to water drop shape was conducted using a contact angle goniometer to evaluate the surface energy of the polymer surface pre- and post-PSE treatment (Figure 4). Surface treatment using Ar^+ plasma on polymer surface like any other plasma treatment has shown to promote surface ablation, crosslinking and activation [23]. The yield of these so-called dangling bonds resulting from the surface treatment is defined by the exposure time and plasma power. Figure 4 shows the measured c.a for both pristine and plasma surface etched polymer surface after 3mins of exposure to Ar^+ plasma. As can be seen, the water c.a measurement for the untreated pristine surfaces for both 3D ABS and Verogray was 40 ° and 58 ° respectively. Nevertheless, after Ar^+ plasma exposure, the respective c.a of both substrates was reduced to 22 ° and 17 ° for both 3D ABS and Verogray respectively. Polymers, in general, have low surface energy, poor wettability and coating adhesion on surfaces are extremely poor after the additive manufacturing process. This is self-evident in the c.a results obtained after the PSE treatment where surfaces possess much higher surface energy as a result of their improved hydrophilicity. Jeon *et al.* [24] in the metallization of PET polymer with Cu showed that pre-treatment is a requirement for stronger adhesion. Lambare *et al.* [25] further showed that the combination of chemical and topographic modification of polymer surface using PSE treatment pre-coating promotes adhesion and mechanical anchoring to the functionalised polymer surface. They further demonstrated a positive correlation between surface wettability and adhesion strength when ABS, ABS/PC and PEEK polymers were treated in an argon plasma for 2 minutes.

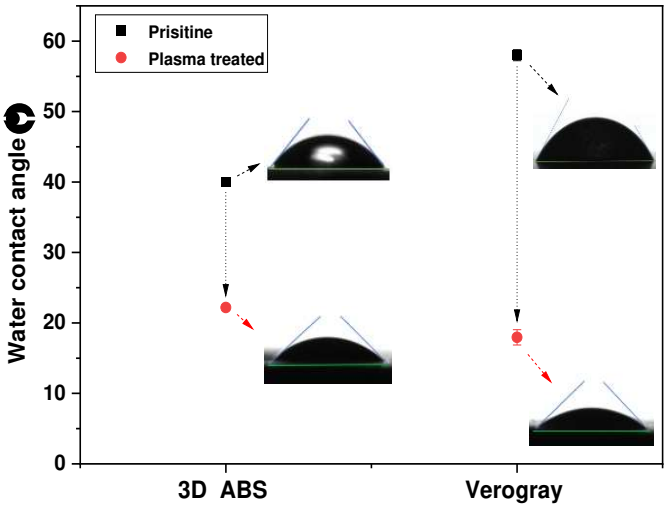

Figure 4- Water contact angle measurement for both pristine and plasma surface etched after 3mins for 3D ABS and Verogray.

3.2. DLC deposition and thin film thickness

The deposition rate for both DLC-1 and DLC-2 films are shown in Figure 5. Additionally, the corresponding SEM micrograph showing the coating thicknesses for both DLC-1 and DCL-2 as deposited on both 3D ABS and Verogray are shown (Figure 5). The substrate temperature at each of the four deposition legs was held at or below 40 °C during the entire deposition run as shown in Figure 6, allowing sufficient film thickness to develop without compromising the polymer structure. During the deposition, the heating rates of all legs were seen to be generally linear, however, where this was not the case, a decrease in the heating rate was observed. This could be ascribed to the difficulty in sustaining the plasma as flow variations were observed for the Ar gas feed. The highest heating rate of 2.9 °C/min was found for DLC-1 as against 1.2 °C/min for DLC-2 during deposition. Nevertheless, the error bars in Figure 6 show that both deposition conditions used produced similar heating rates. Ar and C_2H_2 flow rates were maintained at 50 and 610 sccm respectively at a constant pressure of 0.012 mbar. As seen in Figure 5 (a), it is noticeable that increasing the nitrogen content from 0 sccm to 20 sccm (DLC-2) in the gas mixture produces a monotonic decline in the deposition rate. Sreenivas *et al.* [23] demonstrated the effect of nitrogen doping on the growth and properties of DLC films and noted an inverse relationship between the deposition rate and nitrogen inlet mole fraction. Jonas *et al.* [26] however noted that this decrease in deposition rate is not exclusively linked to the doping effect of nitrogen, but as a consequence of the changes in temperature during deposition. Even though the dissociation of hydrocarbon molecular species produces carbon-rich radicals,

particularly C, CH, CH_2 and CH_3^* species through electron collision with either the gas phase or substrate [23], the active controlling species predominating the build-up and growth of DLC film are the CH_3^* and CH_3 [27]. For a nitrogen-doped DLC film, Amir and Kalish [28] noted that film growth is an exponential function of the total amount of nitrogen present within the gas mixture. However, when hydrogen is present during deposition, the polymeric hydrocarbon (sp^3) content is reduced as a result of the high affinity between the amino group and hydrogen [29]. As a consequence of this fast reaction [23], hydrogen is captured in the process, thus starving the formation of sp^3 cluster fraction within the film. Further analysis using IR absorption spectra in a nitrogen-doped DLC environment with increasing nitrogen content shows an increasing shift in the formation of amino (NH_2) and nitrile (C≡N) containing group over the synthesis of sp^3 molecular species [23].

A comparison between the coated substrate thickness and deposition rate (Figure 5) shows that under similar deposition conditions, film growth is enhanced in all cases for 3D ABS polymers compared with Verogray. The highest coating thickness of 2 µm was observed for DLC-1 on 3D ABS as opposed to a reduced thickness of 1.3 µm for the same material when increasing nitrogen gas flow was utilised (DLC-2). For similar deposition parameters, Verogray, on the other hand, showed a much-reduced coating thickness with the highest of 1.7 µm recorded under DLC-1 and 1.1 µm when coated with DLC-2 film.

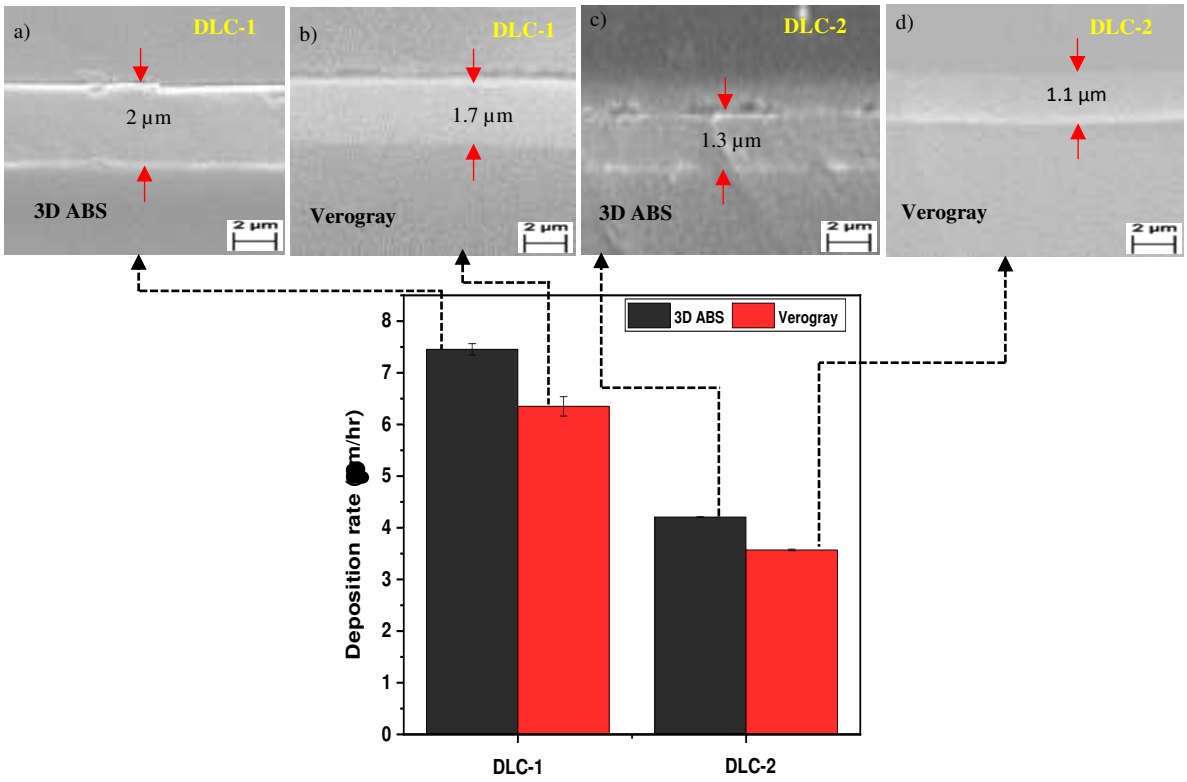

Figure 5- Variation in deposition rate of DLC films with corresponding cross-sectional SEM images showing coating thickness on 3D ABS and Verogray polymer samples.

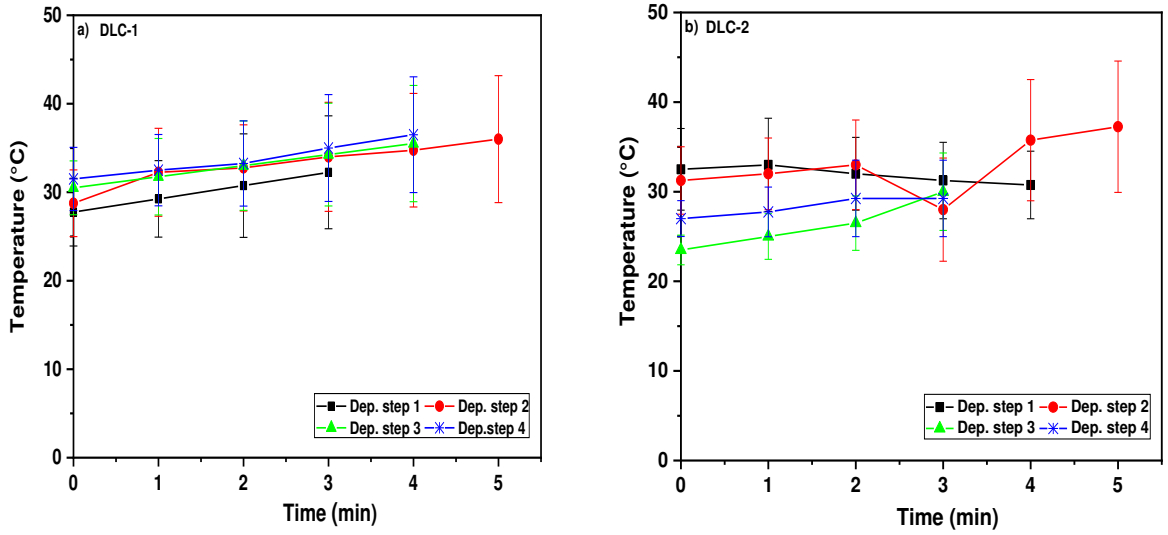

Figure 6- Temperature evolution showing the deposition steps for (a) DLC-1 and (b) DLC-2 as deposited on 3D ABS.

3.3. AFM analysis

3.3.1. *Surface morphology characterisation*

The surface characterisation at the nanoscale, using AFM has proven to be a useful tool in offering both quantitative and qualitative information about material surface properties [30]. Material quantitative properties such as height and surface roughness can easily be probed without damaging the fibrillar structure of the surface [30]. Figure 7 and 8 provide a detailed morphological description of both uncoated and coated surfaces for 3D ABS and Verogray substrates respectively. From Figure 7 and 8, the detailed comparative AFM surface scan showing the material surface properties pre and post coating is made evident. The 3D topography image scale reveals a heterogeneous surface with very low colour variation contrast showing the non-uniformity of surface features on both samples. As a general observation of both 3D ABS and Verogray substrates shown in Figure 7 (a) and Figure 8 (a) respectively, the variation depicted by the colour contrast is self-evident to prove the surface feature disparity present before coating [31]. An important surface feature observed typically with 3D ABS is the presence of micro pit like defects structures (shown in Figure 7 (a) and (b)) [32, 33]. These pit-like structures are seen to be irregularly dispersed on both pristine and coated DLC-1 3D ABS substrate surfaces owing to the deficiency in the photopolymerization process. Jiang *et al*. [34] noted that these defects are created as a result of the volume shrinkage caused by the inherent polymerization strain created between the 3D printed polymer and the base substrate during photo-polymerization, thus creating enough stress through which both micro and macro-pits propagation occur.

As further observed, the differences in peak height values and distribution over the entire surface of the Verogray sample for both coated and uncoated samples show a very heterogeneous surface morphological structure compared with 3D ABS when coated with functional DLC films. For all samples studied, the average surface roughness value of the uncoated substrates was much lower than their coated counterparts, as shown in Figure 9. The average surface roughness on the uncoated 3D ABS and Verogray samples were 1.3 and 0.4 nm respectively. However, by the application of functional DLC coating films onto the 3D polymer surfaces, their average surface roughness increased sharply. With the increment of nitrogen gas incorporation from 0 - 20 sccm, the average roughness increased from 2.6 to 4.7 nm for 3D ABS and 3.5 to 5.1 nm for Verogray.

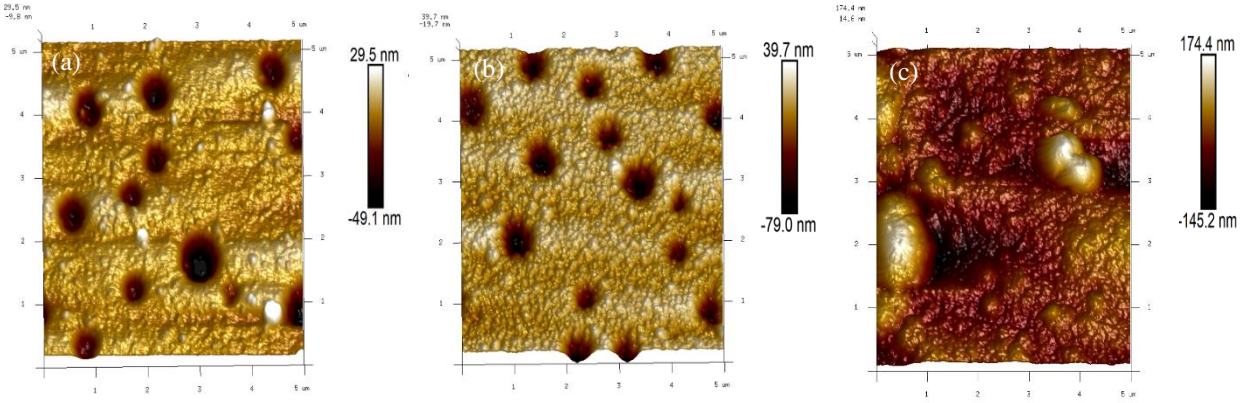

Figure 7- AFM image of 3D ABS polymer surfaces showing (a) uncoated (b) coated with DLC-1 and (c) coated with DLC-2.

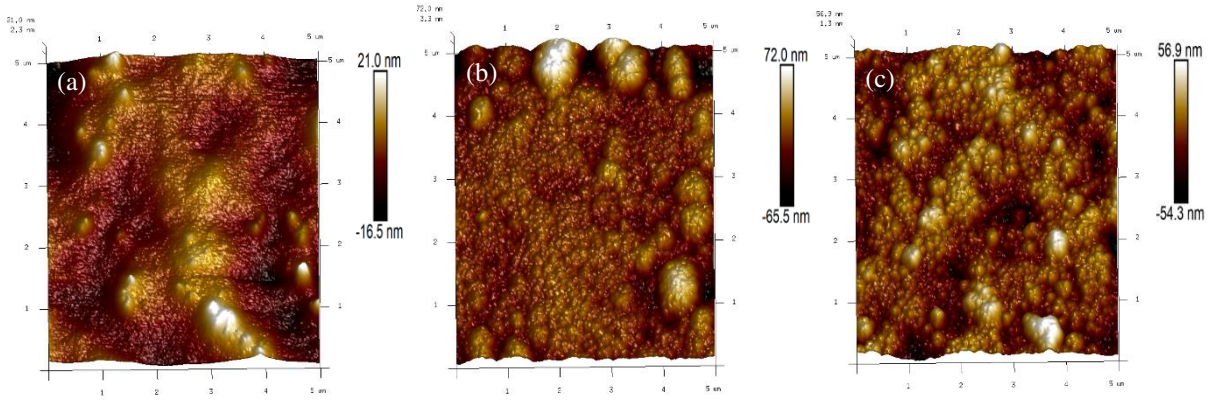

Figure 8- AFM image of 3D Verogray polymer surfaces showing (a) uncoated (b) coated with DLC-1 and (c) coated with DLC-2.

3.3.2. *Coating roughness*

Surface morphology variation due to surface roughness in DLC coatings is affected by the surface species migration, graphitic crystallisation, surface bombardment of energetic particles and surface temperature [35]. Several authors have noted that the growth rate of DLC films decreases with temperature increase [36, 37, 38]. The initial research conclusion was that this was as a result of the weakly adsorbed neutral species which would desorb from the film at higher temperatures [37, 38], but Kessels *et al.* [39], von Keudel and Jacob [40, 41] noted that contrary to the desorption theory of atomic neutral exclusion at higher temperatures, the dependence in film growth at higher temperatures is as a consequence of atomic hydrogen etching effect. Atomistic growth of film is independent of temperature [36]. Aarão Reis and Franceschini [42], in a study of the deposition and erosion model feature of carbon-nitrogen film growth under PECVD, observed an increase in surface roughness of the a-C:N:H film with increasing nitrogen content. They further noted that this increment in surface roughness was because of the erosion driven behaviour facilitated by N_2^+ ion bombardment. Similarly, Silva *et al.* [43] observed an increase in surface roughness with increasing nitrogen incorporation, which is shown to be related to the film growth kinetics during deposition [42]. In this work, when the flow of nitrogen gas is increased in the deposition chamber, the N_2^+ ion bombardment is greatly enhanced, which further facilitates the erosion of the polymer surface and coating structure, thus creating a more uniform surface void of any micro or macro pit-like structures. The resulting coating consequently would promote increasing surface etching causing higher surface roughness for both coatings (Figure 9), with significantly higher deposition rates when nitrogen is incorporated in DLC-2.

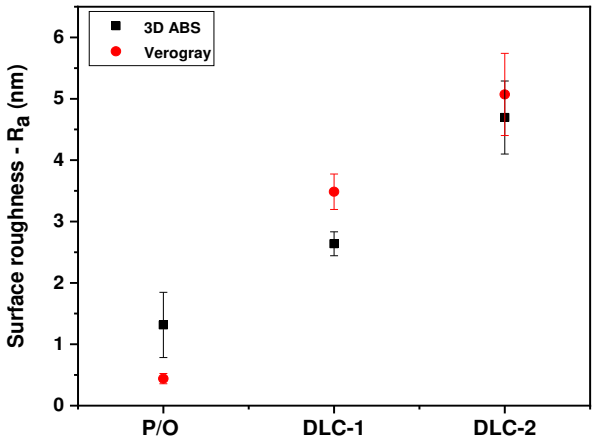

Figure 9- Surface roughness quantification using AFM scan of the individual surfaces. P/O is the pristine uncoated 3D printed samples. DLC-1 and DLC-2 are the coated samples deposited with 0 and 20sccm of Nitrogen flow.

3.4. Raman spectroscopy

The central focal point of any amorphous carbon film is the hybridization of the carbon atom [11]. If a large fraction of sp^3 dominated carbon atoms exists in a well cross-linked DLC film, an improvement in the film hardness is achieved as a result. However, the main concern arises with the hybridization state of carbon atoms when the structure is incorporated with nitrogen. Several authors have reported a decline in the sp^3 C atomic fraction when nitrogen is incorporated as a precursor during deposition [44, 45, 46]. Raman spectroscopy among other useful structural characterisation tools [36] provides useful information about the structural quality of diamond, graphite and DLCs. For this work, Raman spectroscopy was used to characterise the film quality produced by the MW-PECVD technique (Figure 10). As in a-C:H and a-C:N:H films, the main structural features are the broad peaks shown as the 'D' and 'G' bands present in the non-crystalline graphitic carbon material. Both 'D' and 'G' peak modes correspond to the fundamental breathing modes of sp^2 C atoms in rings (A_{1g} mode) and E_{2g} mode of graphite in the bond disordered chain structure [31, 47, 48]. For both DCL-1 and DLC-2 coatings, their corresponding 'D' band peaks were positioned at 1316 and 1326 cm^{-1} wavenumbers whereas their 'G' band peaks were centred at 1530 and 1534 cm^{-1} wavenumbers respectively. This shift in both the 'D' and 'G' band corresponds to the change in the film structure towards a more sp^2 clustering C atom [11]. Menegazzo *et al.* [49], noted similarly a decrease of the full width at half maximum (FWHM) of the G-band upon addition of nitrogen to the DLC structure. From Figure 10, it was indicative of the broadening band manifestation of the D-peak between 1100 and 1600 cm^{-1} even though this broadening feature was much extensive in the DLC film incorporated with nitrogen flow during deposition (DLC-2). Schwan *et al.* [50] and Stan *et al.* [31] both noted that this broadening feature observed between these wave limits are a result of the manifestation of the presence of monocrystalline diamond-like cluster of sp^3 C atomic bonding.

The position and width of both D and G band ratios (I_D/I_G) after spectra deconvolution fitting of the integrated areas under both peaks provide a useful correlation between the sp^3 and sp^2 bonding ratios within the amorphous film [31, 51]. Mariotto *et al.* [52] in a study of a-C:N:H film deposited using rf-PECVD in a methane-nitrogen environment observed that the Raman spectra of the I_D/I_G ratio upon nitrogen doping increases the G peak position towards a more crystalline graphite structure. This phenomenon was attributed to the rise in the graphitic clustering of the sp^2 hybridized carbon atom in agreement with the explanation given by Dillon *et al.* [53].

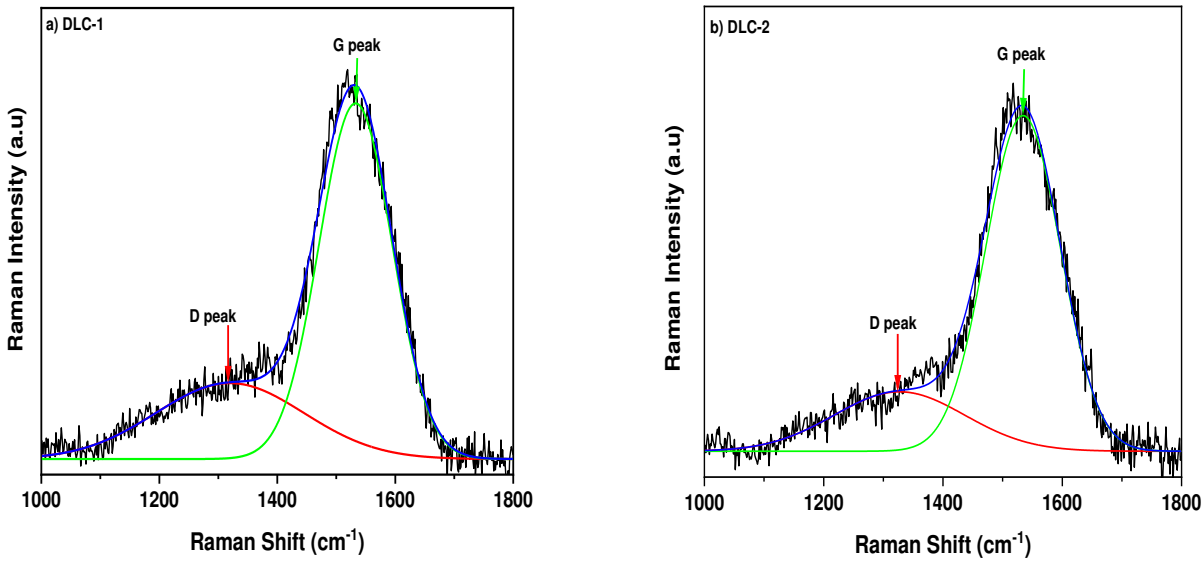

Figure 10- Raman spectra corresponding to DLC films for (a) DLC-1 (b)DLC-2.

3.5. I_D/I_G ratio and coating hardness correlation

To ascertain the accuracy of the I_D/I_G ratio as a measurable quantification of the sp^3/sp^2 content of the DLC films [31], the coating hardness was measured using nanoindentation. As can be seen from Figure 11, increasing the nitrogen gas flow rate from 0 - 20 sccm increases the DLC film hardness for the DLC-2 film deposited on both substrates. Although a greater number of authors have observed decreases in the stress release of most DLC films by the incorporation of nitrogen into the film, the observable mechanical hardness behaviour has shown a widespread performance due to the sp^3 and sp^2 cluster function [11]. Whilst some authors have reported no significant variations in the hardness of DLC films doped with nitrogen at different flow rates [11, 44, 45], others have reported the contrary where significant hardness reduction in DLC films doped with nitrogen is observed [11, 54, 55]. As the nitrogen gas flow increases from 0-20 sccm, one would expect a decrease in the mechanical hardness of the thin film [11, 44, 56], however, the reverse was observed for this work. Thus, further investigations to ascertain the validity of the I_D/I_G ratio to hardness claim was required.

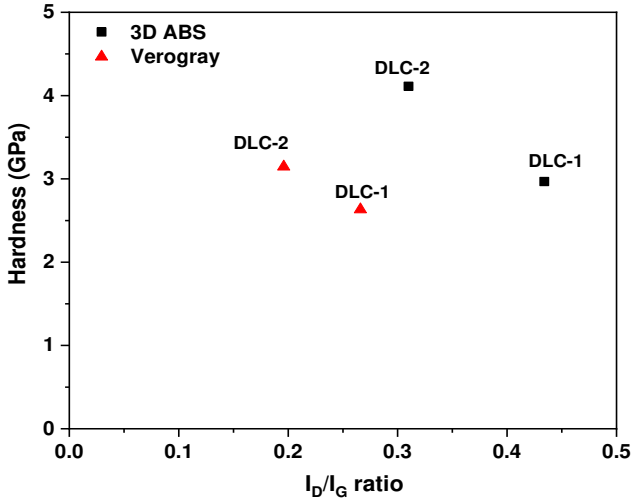

Figure 11- Correlation between I_D/I_G and hardness deposited on both 3D ABS and Verogray.

An elemental compositional analysis using XPS is presented for both C1s and N1s binding state and the compositional percentages for both DLC-1 and DLC-2 are shown in Figure 12. XPS scan at the film surface shows a highly rich C1s atomic concentrated film for DLC-2 which increases with depth until a maximum concentration is attained at 100nm. For DLC-1, the C1s concentration was slightly lower than the DLC-2 (Figure 12 (a)). It was

observed that, as the nitrogen gas flow rate increases from 0-20 sccm, the atomic N1s percentage within the DLC-2 film decreases with depth (Figure 12 (b)). The higher atomic nitrogen percentage fraction observed in DLC-1 could only be possible as a result of the presence of nitrogen impurities in the precursor gas used for the deposition. Acetylene gas possesses great advantages over other precursor gases utilised in plasma deposition such as benzene, butane, methane. Acetylene has high ionisation potential at low pressures, simple dissociation paths are given off mainly $C_2H_n^+$ ions and less polymerisation [36]. However, one of the biggest disadvantages identified with the use of acetylene is the possession of high nitrogen impurity content [36, 57, 58]. Weiler *et al.* [58] after depositing ta-C:H using acetylene gas, noted a 4 % atomic nitrogen content present within the acetylene based DLC film which they attributed to impurities in the acetylene gas.

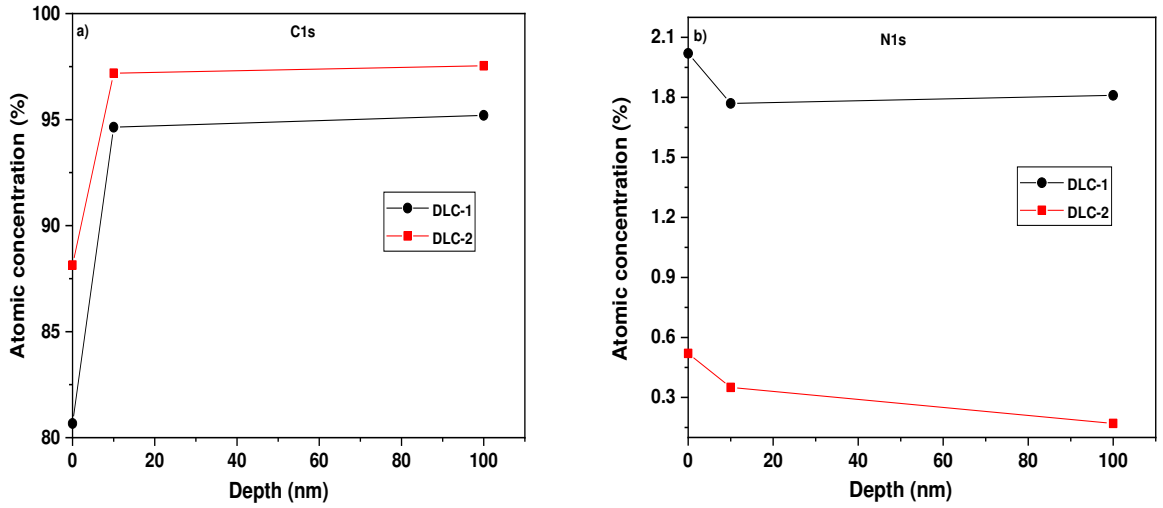

Figure 12- Atomic concentration plot for C1s (a) and N1s (b) as a function of coating depth calculated from XPS spectra deconvolution for both DLC-1 and DLC-2 films as deposited on 3D ABS.

3.6. Coating adhesion

The outcome of the individual scratch test for both DLC-1 and DLC-2 coatings are shown in Figures 13 and 14, respectively. The test results provide a series of multiple failure mechanisms observed as critical failure points of the individual coatings on both 3D ABS and Verogray samples. As Ollivier & Matthews [59] noted, coating failure occurs at different modes owing to the substrate and coating properties, thus critical loads corresponding to the failure points on the coating are used to describe the observed effect. In all cases, the majority of the shape and failure modes suggested predominantly tensile damage with coating spallation failure occurring near the maximum critical load point [60]. The initial critical load values (L_c1) for both coatings were in the range of 0.7 N to ~5 N, depending upon the nitrogen content in the film [11, 44, 56] and surface energy [24, 25]. It was observed that as the nitrogen content decreases within the film (DLC-2), the onset of coating failure (L_c1) as shown in Figures 13 for 3D ABS decreases as a result. For similar coating on Verogray (Figures 14), the onset of L_c1 was observed at a higher load of ~5 N instead of 0.7 N for the 3D ABS substrate. In the case of DLC-1 coating, the L_c1 values were observed in the range of 2.1 N to 4.5 N for both substrates. Similarly, 3D ABS demonstrated lower L_c1 values compared with Verogray. As further observed by Ollivier & Matthews [59], they noted that, when a compressive load is applied on both hard and soft surfaces, the resulting pressure at the contact is consequently low if the contact surface is soft in comparison to a harder surface. Thus, if a certain pressure is needed at the contact area between the coating and film to induce shear stress large enough to cause coating failure, then this yield pressure will be attained at lower loads for harder coatings than for the softer coating. Here, in this case for both coated 3D ABS and Verogray, the coating adhesion performance is positively correlated to the individual coating hardness.

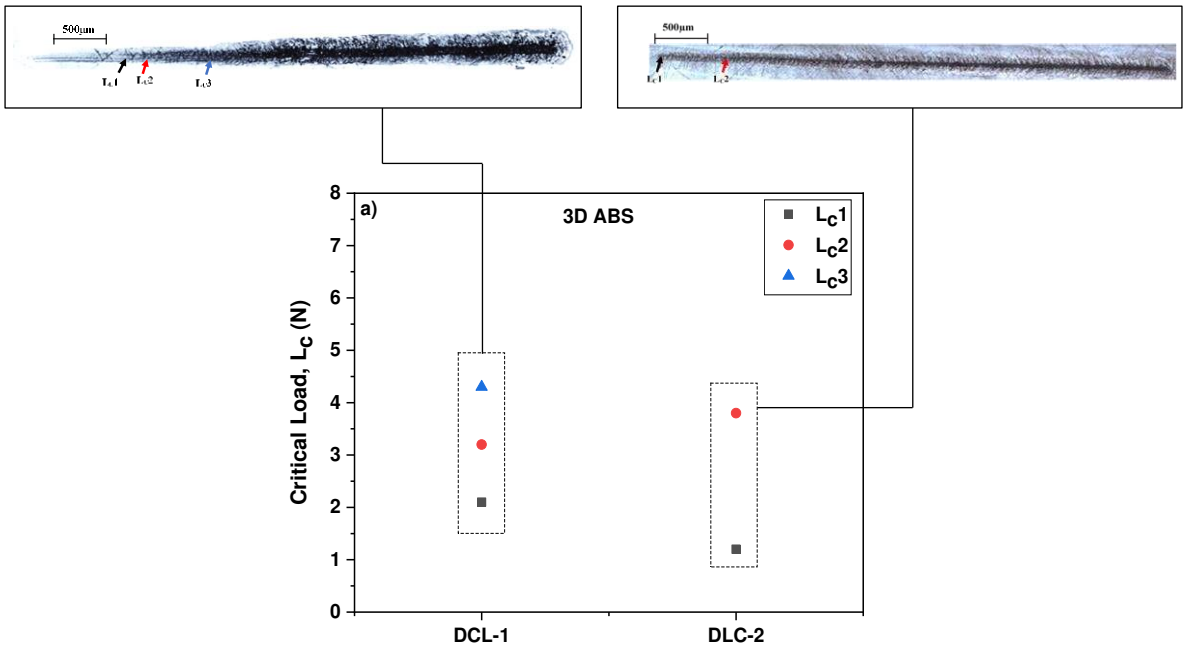

Figure 13- Scratch test results for both DLC-1 and DLC-2 coatings with critical loads, L_c (L_c1, L_c2, L_c3) and film delamination annotation for 3D ABS.

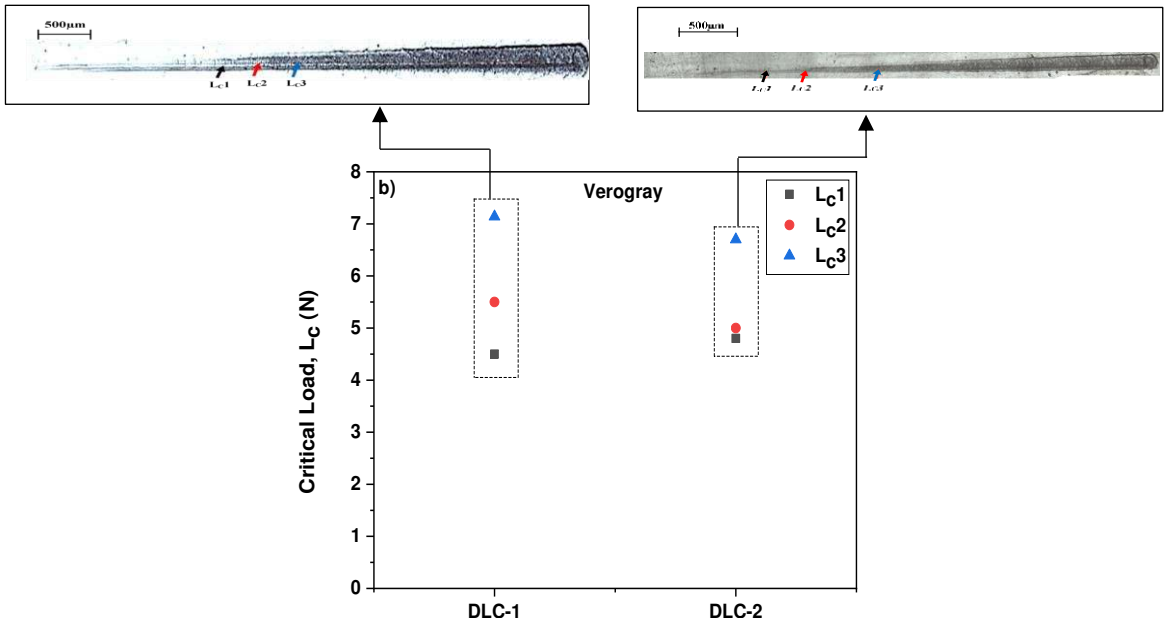

Figure 14- Scratch test results for both DLC-1 and DLC-2 coatings with critical loads, L_c (L_c1, L_c2, L_c3) and film delamination annotation for Verogray.

3.7. Barrier function

Figure 15 shows the various WVTR function curves for both coated and uncoated 3D ABS and Verogray samples. It can be noted that for both uncoated samples, the highest WVTR function was observed. 3D ABS showed the highest WVTR of 73.31 gm/m^2-day in comparison with 28.8 gm/m^2-day for Verogray. This increase observed for the 3D ABS sample can be simply explained by the presence of micro defects within the polymer structure creating diffusion paths for the water vapour molecules to permeate through the polymer matrix. That

notwithstanding, the results also suggest a rather complex diffusion mechanism as the water molecules interact with both 3D ABS and Verogray [61]. The detected porosity and pore size distribution function from the MICP data suggests a large fraction of molecular permeation of water vapour through the pristine sample [62], with the highest expected for 3D ABS, with a 7.7% porosity as opposed to the 6.6% for Verogray, as validated by the WVTR test in Figure 15.

Similarly, Figure 15 shows the measured results of the WVTR function for the coated 3D ABS and Verogray samples. From the 3D ABS plot (Figure 15 (a)), it can be seen that both DLC-1 and DLC-2 films provided improved water barrier performance at 55.68 and 61.51 gm/m^2-day, corresponding to a ~ 24 and ~ 16 % reduction in the WVTR. This is partly due to the role film thickness play in the WVTR reduction [63], by increasing the migration path through which the water molecules would have to travel before being detected by the IR sensory equipment. Ray *et al.* [12] noted that thicker a-C:H films provide a better barrier option for water vapour and oxygen transmission function but cautioned that after a certain thickness, adhesion becomes poor and so does WVTR. As the coating thickness decreases between both DLC films, a corresponding decrease in the WVTR is observed. Furtherance to the role film thickness play in the reduction of WVTR, SEM surface analysis (Figure 16) of the 3D coated sample indicate the presence of micro-crack network spread on both coated 3D ABS substrate surfaces. For the DLC-1 film, the presence of continuous and highly connected micro-crack channels was observed. Abbas *et al.* [63] noted that increasing coating thickness improves barrier performance for DLC coatings on PET unless cracking occur within the coating due to residual stress as thickness increases. As can be seen from Figure 16, it is valid to conclude that, the presence of micro-cracks provides easy access for molecular migration through the DLC coating to the underlying 3D ABD substrate.

Figure 15 (b) presents a comparative plot showing the WVTR function for the pristine (P/O) and coated samples (DLC-1 and DLC-2) for Verogray. It can be observed that the water barrier property of the pristine test sample (Verogray) was significantly reduced when coated with both DLC films. For the DLC-1 and DLC-2 Verogray coated samples, a WVTR of 11.25 and 8.5 gm/m^2-day (Figure 16) was measured. This in comparison with the pristine test sample (Verogray) shows a ~ 60 and ~ 70 % reduction in the WVTR for both DLC-1 and DLC-2 respectively.

The variation in the barrier performance for both coated and uncoated samples as shown in the WVTR plot (Figure 16) indicates that, apart from the bulk material properties, the role of both structural defects and coating adhesion performance at the AM/coating interface plays a significant role in the WVTR function. SEM analysis of both DLC Verogray coated samples showed no surface micro-crack, thus providing a good barrier resistance to water vapour permeation.

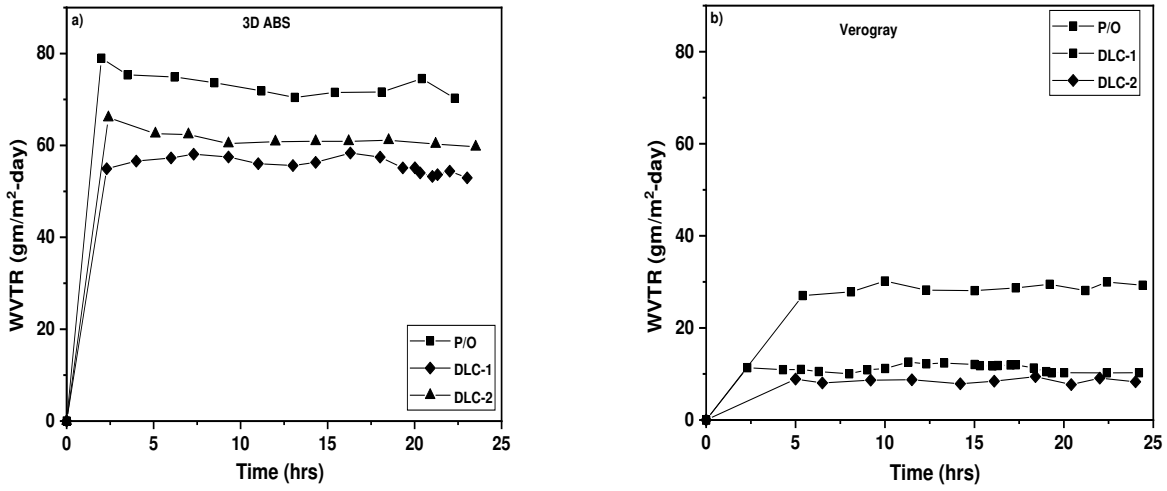

Figure 15- WVTR curve as a function of time for both 3D ABS and Verogray. P/O defines the pristine uncoated 3D ABS (a) and Verogray (b) substrates.

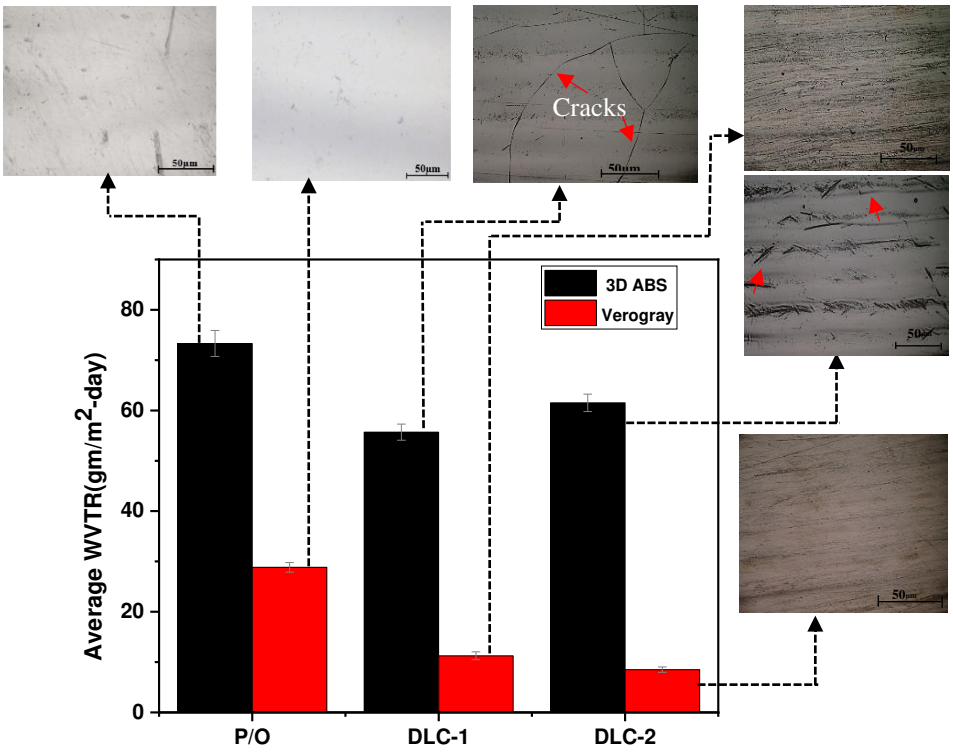

Figure 16- Comparative plot showing the average WVTR rates for ABS and Verogray.

4. Conclusions

In this paper, two a-C:N:H films with varying nitrogen gas flow rates were deposited on 3D ABS and Verogray surfaces by MW-PECVD technique. A combination of Raman analysis, XPS, nanoindentation, and AFM was used to characterise the chemical bonding state, surface chemistry, hardness and microphase separation structures of the DLC coatings. The correlation between the polymer and coating properties on the water barrier performance have been studied. The following summary conclusions are made:

- The relation between the individual film hardness and their corresponding I_D/I_G ratio was seen to be positively correlated with the XPS data where the increase in the nitrogen gas flow rate resulted in increased coating hardness as the nitrogen film composition decreases.
- From the MICP analysis, both 3D ABS and Verogray substrates showed similar pore size distribution function between the meso characterisation range, with 3D ABS showing a higher porosity index of 7.7% than Verogray with an index of 6.6%.
- 3D ABS polymer surface exhibits higher WVTR for both coated and uncoated samples in comparison to Verogray. For the uncoated samples, for example, an average WVTR of 73.31 gm/m^2-day was observed for 3D ABS as opposed to 28.8 gm/m^2-day for Verogray.
- The water permeation results reveal that both DLC films worked as a good barrier against water vapour transmission through the coated samples. For both DLC-1 and DLC-2 coated 3D ABS samples, a WVTR reduction of 24 % and 16 % were recorded. Similarly, the WVTR for the coated Verogray samples showed a 60 % and 70 % reduction for DLC-1 and DLC-2 films respectively.
- Overall, it was shown that Verogray coated samples provided improved barrier protection against water vapour than 3D ABS due to the enhanced coating nucleation at the polymer/coating interface and the lack of micro-pits post-manufacturing.

3D printing is changing the way we interact with product design and performance to unlock the enactment and unparallel deficiencies across various industries, especially within the packaging industry. Even though there are endless possibilities to be harnessed from this technique of 3D manufactured polymers, little research is manifested in these areas, especially in the use of coatings and plasma deposition to enhance the functionality of

these manufactured products. This work has opened a new insight into the understanding of 3D printed material properties and how these properties could be enhanced using plasma-assisted coating technology for specific industrial application such as in the use as a micro seal or for specific atmospheric barrier applications.

In future, further studies could be extended to investigate the correlation between coating adhesion performance and film stress development using varying nitrogen flow rates in accessing the barrier performance for different gases. Additionally, a study on the effect of humidity exposure on the DLC coating structure and performance would be beneficial. Cross-sectional imaging of the coated substrates to ascertain the extent of coating coverage in the micro-pits will provide a better understanding/estimation of the limitations posed by microstructures defects on the WVTR of AM polymers.

Acknowledgements

This work is supported by the Engineering and Physical Science Research Council (EPSRC) through an industrial case studentship with Proctor and Gamble (P&G). The authors would like to extend their gratitude to Sam McMaster and Stuart Micklethwaite of LEMAS (Leeds electron microscopy and spectroscopy centre) for their contribution in preparing this script and producing the SEM cross-sectional images respectively.

References

[1] S. A. M. Tofail, E. P. Koumoulos, A. Bandyopadhyay, S. Bose, L. O'Donoghue and C. Charitidis, "Additive manufacturing: scientific and technological challenges, market update and opportunities," *Materials Today,* vol. 21, no. 1, pp. 22-37, 2018.

[2] Z. Zhang, R. Song, G. Li, G. Hu and Y. Sun, "Improving Barrier Properties of PET by Depositing a Layer of DLC Films on Surface," *Advances in Materials Science and Engineering,* vol. 2013, pp. 1-6, 2013.

[3] J. G. Speight, "Monomers, Polymers, and Plastics," in *Handbook of Industrial Hydrocarbon Processes*, Houston, Gulf Professional Publishing , 2011, pp. 499-537.

[4] A. K. Andrianov and A. Marin, "Degradation of Polyaminophosphazenes: effects of hydrolytic environment and polymer processing," *Biomacromolecules,* vol. 7, no. 5, p. 1581–1586., 2006.

[5] A. Singh, N. R. Krogman, S. Sethuraman, L. S. Nair, J. L. Sturgeon, P. W. Brown, C. T. Laurencin and H. R. Allcock, "Effect of Side Group Chemistry on the Properties of Biodegradable l-Alanine Cosubstituted Polyphosphazenes," *Biomacromolecules,* vol. 7, no. 3, pp. 914-918, 2006.

[6] S. G. Kumbar, S. Bhattacharyya, S. P. Nukavarapu, Y. M. Khan, L. S. Nair and C. T. Laurencin, "In Vitro and In Vivo Characterization of Biodegradable Poly(organophosphazenes) for Biomedical Applications," *Journal of Inorganic and Organometallic Polymers and Materials,* vol. 16, p. 365–385, 2006.

[7] M. Walther, M. Heming and M. Spallek, "Multilayer barrier coating systems produced by plasma-impulse chemical vapour deposition.," *Surface and Coating Technology,* vol. 80, pp. 200-202, 1996.

[8] E. M. Petri, Developments in Barrier Coatings for Plastic Packaging, Surrey: Pira International Ltd, 2006.

[9] T.-Y. Choa, W.-J. Leec, S.-J. Leea, J.-H. Leea, J. Ryud, S.-K. Choa and S.-H. Choab, "Moisture barrier and bending properties of silicon nitride films prepared by roll-to-roll plasma enhanced chemical vapor deposition.," *Thin Solid Films ,* vol. 660, pp. 101-107, 2018.

[10] G. A. Abbas, S. S. Roy, P. Papakonstantinou and J. A. McLaughlin, "Structural investigation and gas barrier performance of diamond-like carbon based filmon polymer susbstrates," *Carbon,* vol. 45, pp. 303-309, 2005.

[11] D. F. Franceschini, "Plasma-deposited a-C(N):H Films.," *Brazilian Journal of Physics,* vol. 3, p. 30, 2000.

[12] S. C. Ray, D. Mukherjee, S. Sarma, G. Bhattacharya, A. Mathurd, S. S. Roy and J. A. McLaughlin, "Functional diamond like carbon (DLC) coatings on polymer for improved gas barrier performance," *Diamond & Related Materials,* vol. 80, p. 59–63, 2017.

[13] M. Ohring, Materials Science of Thin Films, San Diego: Accademic Press , 2002.

[14] Stratasys, "Polyjet 3D Printers," Stratasys, [Online]. Available: https://www.stratasys.com/3d-printers/objet1000-plus. [Accessed 1 March 2019].

[15] F. Dangnan, C. Espejo, T. Liskiewicz, M. Gester and A. Neville, "Friction and wear of additive manufactured polymers in dry contact," *Journal of Manufacturing Processes,* vol. 59, pp. 238-247, 2020.

[16] A. Al Hinai, R. Rezaee, L. Esteban and M. Labani, "Comparisons of pore size distribution: A case from the Western Australian gas shale formations," *Journal of Unconventional Oil and Gas Resources,* vol. 8, pp. 1-13, 2014.

[17] M. Kalin and M. Polajnar, "The correlation between the surface energy, the contact angle and the spreading parameter, and their relevance for the wetting behaviour of DLC with lubricating oils," *Tribology International,* vol. 66, pp. 225-233, 2013.

[18] V. Galstyan, "Porous TiO2-based gas sensors for cyber chemical systems to provide security and medical diagnosis," *Sensors,* vol. 17, no. 12, p. 2947, 2017.

[19] X. Wang, L. Zhao, J. Y. H. Fuh and H. P. Lee, "Effect of Porosity on Mechanical Properties of 3D Printed Polymers: Experiments and Micromechanical Modeling Based on X-Ray Computed Tomography Analysis," *Polymers (Basel),* vol. 11, no. 7, p. 1154, 2019.

[20] D. O. Hummel and F. Scholl, Infrared analysis of polymers, resins and additives: An atlas of polymer and plastic analysis, München: Weinheim/Carl Hanser Verlag, 1978.

[21] B. Stuart, "Infrared spectroscopy: Fundamentals and applications," [Online]. Available: http://www.kinetics.nsc.ru/chichinin/books/spectroscopy/Stuart04.pdf. [Accessed 20 March 2017].

[22] P. R. Griffiths and J. A. de Haseth, Fourier Iransform Infrared Spectrometry, New York: Wiley, 1986.

[23] G. Sreenivas, S. S. Ang and W. D. Brown, "Effects of nitrogen doping on the growth and properties of plasma-enhanced chemical-vapor-deposited diamond-like-carbon films," *Journal of Electronic Materials.,* vol. 23, no. 6, p. 569–575, 1994.

[24] B. J. Jeon, S. Lee and J. K. Lee, "Adhesion characteristics of copper thin film deposited on PET substrate by electron cyclotron resonance–metal organic chemical vapor deposition," *Surface and Coating Technology,* vol. 202, no. 9, pp. 1839-1846, 2008.

[25] C. Lambare, P.-Y. Tessier, F. Poncin-Epaillard and D. Debarnot, "Plasma funtionalization and etching for enhancing metal adhesion onto polymeric substrates," *Royal Society of Chemistry,* vol. 5, pp. 62348-62357, 2015.

[26] S. Jonas, K. Kyzioł, J. Lis and K. Tkacz-Śmiech, "Stability of a-C:N:H layers deposited by rf plasma enhanced CVD.," *Solid State Phenomena,* Vols. 147-149, p. 738–743, 2009.

[27] S. S. Ang, G. Sreenivas, W. D. Brown, N. H. A and U. R. K, "Effects of nitrogen trifluoride on the growth and properties of plasma-enhanced chemical-vapor-deposited diamond-like carbon films," *Journal of Electronic Materials,* vol. 22, p. 347–352, 1993.

[28] O. Amir and R. Kalish, "Properties of nitrogen-doped amorphous hydrogenated carbon films," *Journal of Applied Physics,* vol. 70, pp. 4958-4962, 1991.

[29] J. H. Kaufman, S. Metin and D. D. Saperstein, "Symmetry breaking in nitrogen-doped amorphous carbon: Infrared observation of the Raman-active G and D bands," *The American Physical Society,* vol. 39, no. 18, pp. 053-060, 1989.

[30] A. Stylianou, D. Yova and K. Politopoulos, "Atomic force microscopy quantitative and qualitative nanoscale characterization of collagen thin films. Emerging Technologies in Non-Destructive Testing," *V-Proceedings of the 5th Conference on Emerging Technologies in NDT,* vol. 10, no. 1201/b11837-75., pp. 415-420, 2012.

[31] G. E. Stan, D. A. Marcov, A. Popa and M. A. Chusan, "Polymer-like and diamond-like carbon coatings prepared by rf-pecvd for biomedical applications," *Digest Journal of Nanomaterials and Biostructures,* vol. 5, no. 3, p. 705 – 718, 2010.

[32] E. G. Gordeev, A. S. Galushko and V. P. Ananikov, "Improvement of quality of 3D printed objects by elimination of microscopic structural defects in fused deposition modelling," 07 06 2018. [Online]. Available: https://doi.org/10.1371/journal.pone.0198370. [Accessed 01 01 2021].

[33] J. Fastowicz, M. Grudzinski, M. Tecław and K. Okarma, "Objective 3D Printed Surface Quality Assessment Based on Entropy of Depth Maps," *Entropy,* vol. 21, no. 97, pp. 1-13, 2019.

[34] T. Jiang, Y. He, Y. Jian and J. Nie, "Exploration for decreasing the volume shrinkage for photopolymerization," *Progress in Organic Coatings,* vol. 75, no. 4, p. 398–403, 2012.

[35] M. Constantinou, M. Pervolaraki, P. Nikolaou, C. Prouskas, P. Patsalas, P. Kelires, J. Giapintzakis and G. Constantinides, "Microstructure and nanomechanical properties of pulsed excimer laser deposited DLC: Ag films: enhanced nanotribological response," *Surf. Coat. Technol,* vol. 309, pp. 320-330, 2017.

[36] J. Robertson, "Diamond-Like Amorphous carbon," *Material science and Engineering,* vol. 37, pp. 129-281, 2002.

[37] W. Möller, "Plasma and surface modeling of the deposition of hydrogenated carbon films from low-pressure methane plasmas," *Applied Physics ,* vol. A 56, pp. 527-546, 1993.

[38] W. Möller, W. Fukarek, K. Lange, A. von Keudell and W. Jacob, "Mechanisms of the deposition of hydrogenated carbon films," *Japan Society of Applied Phyiscs,* vol. 34, no. 4S, pp. 2163-2171, 1995.

[39] W. M. M. Kessels, J. W. A. M. Gielen, M. C. M. van de Sanden, L. J. van Ijzendoom and D. C. Schram, "A model for the deposition of a-C:H using an expanding thermal arc," *Surface and Coatings Technology,* vol. 98, no. 1-3, pp. 1584-1589, 1998.

[40] A. von Keudel and W. Jacob, "Growth and erosion of hydrocarbon films investigated by in situ ellipsometry," *Journal of Applied Physics,* vol. 79, pp. 1092-1098, 1996.

[41] A. von Keudel and W. Jacob, "Surface relaxation during plasma-enhanced chemical vapor deposition of hydrocarbon films, investigated by in situ ellipsometry," *J. Appl. Phys.,* vol. 81, pp. 1531-1535, 1997.

[42] F. D. A. Aarão Reis and D. F. Franceschini, "Statistical models for carbon-nitrogen film growth," *American Physical Society,* vol. 61, no. 4, pp. 3417-3425, 2000.

[43] S. R. P. Silva, G. A. J. Amaratunga and J. R. Barnes, "Self-texturing of nitrogenated amorphous carbon thin films for electron field emission," *Applied physics letters,* vol. 71, pp. 1477-1479, 1997.

[44] D. F. Franceschini, F. L. J. Freire and S. R. P. Silva, "Influence of precursor gases on the structure of plasma deposited amorphous hydrogenated carbon–nitrogen films," *Journal of Applied Physics,* vol. 68, pp. 2645-2647, 1996.

[45] S. Bhattacharyya, C. Vallé, C. Cardinaud, O. Chauvet and G. Turban, "Studies on structural properties of amorphous nitrogenated carbon films from electron energy loss, ellipsometry, Auger electron spectroscopy, and electron-spin resonance," *Journal of Applied Physics,* vol. 85, pp. 2162-2169, 1999.

[46] V. Veerasamy, J. Yuan, G. Amaratunga, W. Milne, K. Gilkes, M. Weiler and L. Brown, "Nitrogen doping of highly tetrahedral amorphous carbon," *Physical Review B,* vol. 48, no. 24, pp. 17954-17959, 1993.

[47] A. C. Ferrari and J. Robertson, "Origin of the 1150-cm-1 Raman mode in nanocrystalline diamond," *PHYSICAL REVIEW B,* vol. 63, no. 362, pp. 121405-1 - 121405-4, 2001.

[48] A. C. Ferrari and J. Robertson, "Resonant Raman spectroscopy of disordered, amorphous, and diamondlike carbon," *Physical Review B,* vol. 64, pp. 075414-1 - 075414-13, 2001.

[49] N. Menegazzo, R. Berghauser, W. Waldhauser and B. Mizaikoff, "Nitrogen-doped diamond-like carbon as optically transparent electrode for infrared attenuated total reflection spectroelectrochemistry," *Analyst,* vol. 136, pp. 1831-1839, 2011.

[50] J. Schwan, S. Ulrich, V. Batori and H. Ehrhardt, "Raman spectroscopy on amorphous carbon films," *Journal of Applied Physics,* vol. 80, pp. 440-447, 1996.

[51] C. Liu, D. Hu, J. Xu, D. Yang and Q. Min, "In vitro electrochemical corrosion behavior of functionally graded diamond-like carbon coatings on biomedical nitinol alloy," *Thin Solid Films,* vol. 257, p. 496, 2006.

[52] G. Mariotto, F. L. J. Freire and C. Achete, "Raman spectroscopy on nitrogen-incorporated amorphous hydrogenated carbon films," *Thin Solid Films,* vol. 241, p. 255, 1994.

[53] R. O. Dillon, J. A. Woolam and V. Katkanant, "Use of Raman scattering to investigate disorder and crystallite formation in as-deposited and annealed carbon films," *Phys. Rev.,* vol. B29, p. 3482, 1984.

[54] J. Schwan, W. Dworschak, H. Jung and H. Ehrardt, "Microstructures and mechanical properties of amorphous hydrogenated carbon-nitrogen films," *Diamond and Related Materials,* vol. 3, no. 7, pp. 1034-1039, 1998.

[55] P. Wood, T. Wyedeven and O. Tsuji, "Plasma-deposited aC (N): H films," *Thin Solid Films,* vol. 258, no. 1-2, pp. 151-158, 1995.

[56] K.-R. Lee, K. Eun and J. S. Rhee, "Structure and mechanical properties of nitrogen incorporated diamond-like carbon films," *Mat. Res. Soc. Symp. Proc.,* vol. 356, no. 233, pp. 233-238, 1995.

[57] N. M. J. Conway, A. C. Ferrari, A. J. Flewitt, J. Robertson, W. I. Milne, A. Tagliaferro and W. Beyer, "Defect and disorder reduction by annealing in hydrogenated tetrahedral amorphous carbon," *Diamond and Related Materials,* vol. 9, no. 3-6, pp. 765-770, 2000.

[58] M. Weiler, S. Sattel, T. Giessen, K. Jung, H. Ehrhardt, V. S. Veerasamy and J. Robertson, "Preparation and properties of highly tetrahedral hydrogenated amorphous carbon," *Phys. Rev. B,* vol. 53, pp. 1595-1607, 1996.

[59] B. Ollivier and A. Matthews, "Adhesion of diamond-like carbon films on polymers: an assessment of the validity of the scratch test technique applied to flexible substrates.," *J. Adhesion Sci. Technol,* vol. 8, no. 6, pp. 651-662, 1994.

[60] S. J. Bull, "Failure modes in scratch adhesion testing," *Surfaceand Coatings Technology,* vol. 50, pp. 25-32, 1991.

[61] A. S. da Silva Sobrinho, G. Czeremuszkin, M. Latrèche and M. R. Wertheimer, "Defect-permeation correlation for ultrathin transparent barrier coatings on polymers," *Journal of Vacuum Science & Technology,* vol. A 18, pp. 149-157, 2000.

[62] A. Perrotta, G. Aresta, E. R. J. van Beekuma, J. Palmans, P. van de Weijer, M. R. van de Sandenc, W. E. Kessel and M. Creatore, "The impact of the nano-pore filling on the performance of organosilicon-based moisture barriers," *Thin Solid Films,* Vols. 595, Part B, pp. 251-257, 2015.

[63] G. Abbas, P. Papakonstantinou, T. I. T. Okpalugo and J. A. McLaughlin, "The improvement in gas barrier performance and optical transparency of DLC-coated polymer by silicon incorporation," *Thin Solid Films,* Vols. 482(1-2), pp. 201-206, 2005.